



Fracture modelling of adhesively-bonded joints by an inverse method

F.A.L. Viana

Departamento de Engenharia Mecânica, Instituto Superior de Engenharia do Porto, Instituto Politécnico do Porto, Portugal
1120367@isep.ipp.pt

R.D.S.G. Campilho

Departamento de Engenharia Mecânica, Instituto Superior de Engenharia do Porto, Instituto Politécnico do Porto, Portugal
INEGI – Pólo FEUP
raulcampilho@gmail.com, <https://orcid.org/0000-0003-4167-4434>

R.J.B. Rocha

INEGI – Pólo FEUP, Portugal
ricardojbragarocha@gmail.com

D.F.O. Silva, R.V.C. Araújo, J.P.S.M.B. Ribeiro

Departamento de Engenharia Mecânica, Instituto Superior de Engenharia do Porto, Instituto Politécnico do Porto, Portugal
1060548@isep.ipp.pt, 1980512@isep.ipp.pt, 1120523@isep.ipp.pt



ABSTRACT. Nowadays, any structure must have strength, robustness and lightness, which has increased the industrial interest and research efforts in adhesive joining, mainly in the improvement of strength and fracture properties of adhesives. Thus, in recent years, the use of adhesive joints in industrial applications has gradually grown, replacing some traditional bonding methods, since they have advantages such as reduced stress concentrations, reduced weight and cost, and ease of processing/manufacturing. In this work, the cohesive laws of three adhesives, Araldite® AV138, Araldite® 2015 and Sikaforce® 7752, were obtained by the application of an inverse adjustment method between the numerical and experimental load-displacement curves ($P-\delta$) of Double-Cantilever Beam (DCB) tests for tensile characterization and End-Notched Flexure (ENF) tests for shear characterization. Next, these laws were validated with experimental data of single-lap joints (SLJ) and double-lap joints (DLJ), using Abaqus®. For the Araldite® AV138 and Araldite® 2015, in tension and shear, the triangular law accurately predicted the behaviour of the SLJ and DLJ. For the Sikaforce® 7752, the triangular law did not suitably fit the experimental results. Due to its ductility, the Sikaforce® 7752 could be modelled with a trapezoidal law for improved accuracy.

Citation: Viana, F.A.L., Campilho, R.D.S.G., Rocha, R.J.B., Silva, D.F.O., Araújo, R.V.C., Ribeiro, J.P.S.M.B., Fracture modelling of adhesively-bonded joints by an inverse method, *Frattura ed Integrità Strutturale*, 48 (2019) 286-303.

Received: 24.09.2018

Accepted: 03.01.2019

Published: 01.04.2019

Copyright: © 2019 This is an open access article under the terms of the CC-BY 4.0, which permits unrestricted use, distribution, and reproduction in any medium, provided the original author and source are credited.



KEYWORDS. Adhesive joint; Structural adhesive; Cohesive zone models; Inverse method; Parameter identification.

INTRODUCTION

Adhesive is a substance that joints two materials together, known as adherends, in a strong and permanent way [1]. Bonding is by far the most universal joining technique. Essentially, all useful materials can be joined throughout this surface-to-surface joining technique. Adhesive bonding has been used as a joining technique since 4000 b.C. by the Mesopotamians, using asphalt for constructions [2]. In the early 1900s, synthetic polymeric adhesives replaced natural ones, giving products with stronger adhesion and superior resistance [1]. The aviation and aerospace industries, with their inherent history of innovation, novel designs and technologies, were the ones that most contributed for the widespread use of adhesive bonding. From the very early days of structural adhesives, they have been used in order to enable the construction of lighter, stronger and more long-lasting airframes and aircrafts. Major advantages of adhesively-bonded joints are the possibility to join different materials, more uniform stress fields along the bonded area, more efficient load transfer, fluid sealing, corrosion resistance, high fatigue strength and better aesthetics (without bolts heads, rivets or welding). On the other hand, as disadvantages one may refer the need of the joint design to be oriented towards the elimination of peel stresses, low resistance to temperature and humidity and the requirement of a surface treatment [1, 3]. In an ideal joint, the adhesive should be only subjected to shear stresses and the load-bearing area should be as large as possible but, due to design limitations, this cannot always be applied [4]. Different joint architectures give the engineers a wide range of solutions depending on the application. SLJ are easy to manufacture, can be used with thin adherends and the adhesive is mostly loaded by shear (τ_{xy}) stresses. However, the adherends are not collinear, which leads to significant peel (σ_y) stresses at the overlap end [1]. On the other hand, DLJ have a balanced construction that decreases the bending moment. Nonetheless, the internal bending moments cause peel stresses at the ends of the inner adherend. Recent solutions included wavy and reverse-lap joints. Avila and Bueno [5] evaluated the wavy-lap joint architecture and concluded that the maximum load (P_m) supported by those joints was in average 41% higher than that carried by equivalent SLJ. Scarf joints' manufacture is difficult due to the adherends' tapering at the bond region. However, this design keeps the axis of loading in line with the joint, which is prone to reduce σ_y stresses in the adhesive layer. Thus, these joints endure higher strengths compared with the above-mentioned lap joints, for the same bonded area.

Undoubtedly, it is necessary to provide accurate tools to predict the strength, possible points and paths of failure of adhesive joints. This is essential to enable the widespread applicability of this technology in different industrial fields. This quest began about eighty years ago with a simple analytical analysis of SLJ performed by Volkersen [6]. However, the analysis requirement of several joint designs and novel adhesives with high plasticity degree, rendered the analytical analyses unpractical. The development of Finite Element (FE) techniques brings new horizons to the P_m prediction of bonded joints, notwithstanding the design, load conditions and adhesives' plasticity. Among several approaches, the cohesive zone modelling (CZM) technique, presented by Barenblatt [7] and Dugdale [8], is currently the most used. This method relies on the establishment of tensile and shear traction-separation laws, linking the cohesive tractions (t_n for tension and t_s for shear) with the relative displacements (δ_n for tension and δ_s for shear). Moreover, different criteria to assess mixed-mode damage initiation and growth are used. Using this methodology, damage is simulated along a predefined crack path, which can be an inconvenient if this path is not known beforehand. However, in bonded joints this does not constitute a limitation, since failure is usually confined to the adhesive layer and respective interfaces, or in the worst case to parallel adherend delaminations when using composite adherends [9]. Provided that the modelling conditions are properly established for a specific structure and that the cohesive parameters, namely, the shear cohesive strength (t_s^0), the tensile cohesive strength (t_n^0), the fracture toughness in tension (G_{IC}) and shear (G_{IIC}), are accurately characterized, CZM is a precise technique for strength prediction of adhesively-bonded joints [10]. Thus, one must assure the correct determination of the cohesive parameters. For that purpose, one possible method is the property identification technique, which estimates each one of the cohesive law parameters by suitable tests [9]. On the other hand, the direct method provides the precise shape and the complete CZM laws because it uses experimental data from the DCB or ENF fracture tests. This is accomplished through the differentiation of the fracture energy in tension (G_I) or the fracture energy in shear (G_{II}) with respect to δ_n or δ_s , respectively [11]. The inverse method consists of the estimation of the CZM parameters by iterative fitting the numerical prediction with experimentally measured data (typically the P - δ curve), considering a precise description of the experimental geometry and approximated cohesive laws. The inverse characterization of adhesive bonds should be applied individually for each tested specimen to account for slight geometry variations between specimens. The value of G_{IC} or G_{IIC} , usually

determined by DCB and ENF tests, respectively, are initially used in the respective CZM law. Concurrently, approximate bulk values can be used for t_n^0 or t_n^0 for the initiation of the trial and error iterative process. Examples of experimental data for the iterative fitting procedure are the R -curve, the crack opening profile and the P - δ curve [12].

Xu et al. [13] developed an improved interpolation-based CZM model to capture the tensile behaviour of different fracture scenarios in composite adhesive joints, using the DCB specimen. Simultaneously, an inverse method was developed to assess the tensile CZM parameters. This inverse analysis relies upon both experimental P - δ curves and displacement distribution in the neutral layer of bending beam. The numerical CZM simulations, and an optimization algorithm capable to approach the simulations to the experimental results, enabled obtaining the optimal tensile CZM parameters. Throughout experimental data, the model was validated, showing the reliability of the proposed solution. Azevedo et al. [14] estimated the CZM laws of adhesively-bonded joints subjected to shear loading through the inverse method based on a curve fitting procedure. Three adhesives with different ductility grades were used to bond aluminium adherends. To estimate the shear CZM laws, ENF tests were carried out. G_{IIC} was used to build a triangular CZM law to begin the iterative process and then iterations were performed, by fitting the experimental and numerical P - δ curves, to estimate t_s^0 . During the fitting process, it was shown that the Young's modulus (E) affects the elastic part of the curve, G_{IIC} affects the maximum load (P_m), while t_s^0 changes P_m and highly affects the specimen's stiffness up to the P_m , leading to a more sudden post peak load reduction with the increase of t_s^0 [23]. After application of this process to all specimens, the authors concluded that a unique shear CZM law could be found for each specimen. Moreover, the triangular CZM managed to capture with accuracy the adhesive layer behaviour for all adhesives tested. In the study of Bouhala et al. [15], an inverse method has been also applied to unidirectional carbon fibre-reinforced/epoxy matrix composite failure, showing a trustworthy determination of the tensile failure parameters.

In this work, the cohesive laws of three adhesives, Araldite® AV138, Araldite® 2015 and Sikaforce® 7752, were obtained by the application of an inverse adjustment method between the numerical and experimental P - δ curves of DCB tests for tensile characterization and ENF tests for shear characterization. Next, these laws were validated with experimental data of SLJ and DLJ, using Abaqus®.

WORK METHODOLOGY

Aiming to define the tensile and shear CZM laws of the three studied adhesives, enabling their subsequent use for strength prediction of adhesively-bonded joints, the following methodology was followed:

- G_{IC} and G_{IIC} of the three adhesives were experimentally estimated by robust fracture tests such as the DCB and ENF, respectively, and the Compliance-Based Beam Method (CBBM);
- A numerical data fitting process was undertaken, in which individual DCB and ENF models were constructed, with the input G_{IC} and G_{IIC} of each specimen and reference values of the other CZM parameters. The CZM law of each test (either tensile or shear) was individually found by iteratively adjusting, using a trial and error procedure, the reference CZM parameters until the best match is found between the experimental and numerical P - δ curves of the fracture tests;
- Validation of the obtained CZM laws, which is an essential step to enable the design of bonded joints by this process, is divided into three steps: (1) joint stress analysis, which is used to provide a discussion on the P_m differences between joint types, geometry and adhesive type, (2) performing experimental tests and provide the respective discussion, to enable further comparison with numerical models for validation of the CZM laws, and (3) experimental and numerical P_m comparison for all tested conditions which, if positively accomplished, will give the basis for subsequent design of joints bonded with the three adhesives.

EXPERIMENTAL WORK

Adherends and adhesives

The aluminium alloy AA6082 T651 is the material chosen for the DCB, ENF, SLJ and DLJ adherends. This material is a high strength and ductile aluminium alloy, which enables measurement of the CZM laws by the respective fracture tests without evidence of plasticization, which otherwise would result in errors of property estimation. The relevant mechanical properties of this alloy were established in the work of Campilho et al. [16]: E of 70.07 ± 0.83 GPa, tensile yield stress (σ_y) of 261.67 ± 7.65 MPa, ultimate tensile strength (σ_t) of 324 ± 0.16 MPa and tensile failure strain (ϵ_f) of

21.70±4.24%. The experimental tests are done with three structural adhesives: the brittle epoxy Araldite® AV138, the ductile epoxy Araldite® 2015 and the ductile polyurethane Sikaforce® 7752, to evaluate different behaviours and types of failure. These properties were defined in previous works [16-18]. The measurement of E , σ_y , σ_f and ε_f was done by bulk specimens with dogbone shape. The specimens were fabricated following the French Standard NF T 76-142 in a custom mould for simultaneous production of six specimens. Shear characterization was performed by Thick Adherend Shear Tests (TAST). The DCB test was used for G_{IC} and the ENF test was used for G_{IIC} . The manufacture of these specimens was similar to that described in the work of Fernandes and Campilho [19] and curing was done in one week at room temperature. The collected data of the adhesives is summarized in Tab. 1.

Property	AV138	2015	7752
Young's modulus, E [GPa]	4.89±0.81	1.85±0.21	0.49±0.09
Poisson's ratio, ν	0.35 ^a	0.33 ^a	0.30 ^a
Tensile yield stress, σ_y [MPa]	36.49±2.47	12.63±0.61	3.24±0.48
Ultimate tensile strength, σ_f [MPa]	39.45±3.18	21.63±1.61	11.48±0.25
Tensile failure strain, ε_f [%]	1.21±0.10	4.77±0.15	19.18±1.40
Shear modulus, G [GPa]	1.81 ^b	0.70 ^b	0.19 ^b
Shear yield stress, τ_y [MPa]	25.1±0.33	14.6±1.3	5.16±1.14
Ultimate shear strength, τ_f [MPa]	30.2±0.40	17.9±1.8	10.17±0.64
Shear failure strain, γ_f [%]	7.8±0.7	43.9±3.4	54.82±6.38
Toughness in tension, G_{IC} [N/mm]	0.20 ^c	0.43±0.02	2.36±0.17
Toughness in shear, G_{IIC} [N/mm]	0.38 ^c	4.70±0.34	5.41±0.47

^a manufacturer's data

^b estimated from the Hooke's law using E and ν

^c estimated in reference [16]

Table 1: Mechanical and fracture properties of the adhesives Araldite® AV138, Araldite® 2015 and Sikaforce® 7752 [16-18].

Experimental details

The geometry and dimensions of the DCB and ENF specimens are depicted in Fig. 1.

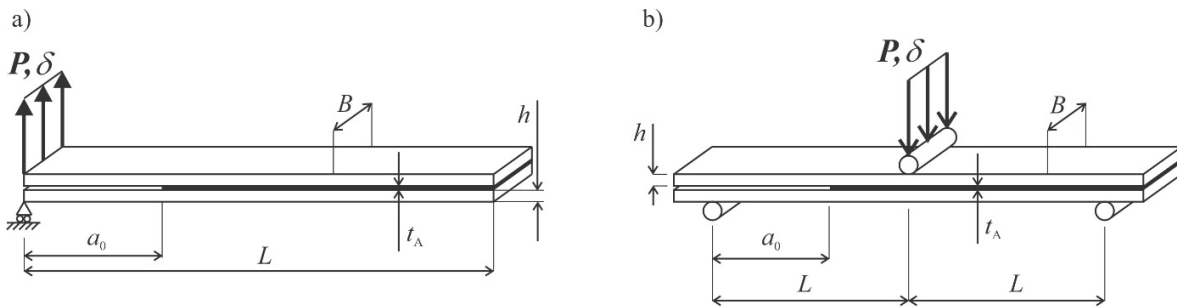


Figure 1: Geometry and dimensions of the DCB (a) and ENF specimens (b).

The main parameters are the total length $L=140$ mm (DCB) or mid-span length $L=100$ mm (ENF), initial crack length $a_0 \approx 40$ mm (DCB) or ≈ 60 mm (ENF), adherends thickness $h=3$ mm, width $B=25$ mm and $t_A=0.2$ mm [20, 21]. The geometry and dimensions of the SLJ and DLJ are described in Fig. 2. The parameters are the following: joint length between grips $L=180$ mm, $h=3$ mm, $B=25$ mm, $t_A=0.2$ mm and overlap length $L_O=12.5, 25, 37.5$ and 50 mm.

The fabrication details presented here are divided into fracture and lap tests, due to the different procedures undertaken. Nonetheless, all specimens were fabricated at room temperature and with approximately 75% of relative humidity, and the respective bonding surfaces were abraded by grit blasting with corundum sand, degreased with acetone, and introduced in a steel mould for bonding. For the specific case of the DCB and ENF specimens, six specimens were fabricated for each joint configuration. For these specimens, calibrated steel spacers were placed between the lower and upper adherends to have the correct value of t_A . To promote an easy extraction after curing the adhesive, these spacers were coated with demoulding agent. The spacers at the crack tip were composed of a sharp razor blade with a thickness of 0.1 mm in-between

two 0.05 mm spacers, to produce the total t_A . The adhesive was poured on one of the adherends, the joints were assembled and pressure was applied up to the adherends contacting the spacers. The mould was closed for curing the adhesive during one week. After this procedure, the spacers were removed, the excess adhesive trimmed, and one of the adherends sides was painted with white paint to measure the crack length (a), and a numbered scale was attached to both adherends in the painted side to follow the crack during the test. To prevent possible crack-tip blunting effects, before measuring a_0 in each specimen the crack was manually propagated in opening mode by a length between 1 and 3 mm and only then a_0 was measured.

For each joint L_0 , five joints were manufactured and tested, either for. In total, 60 SLJ and 60 DLJ were tested. In this work, identical b values were considered for the inner and outer adherends, opposed to using cross-section balanced adherends at both sides of the bond region, i.e., considering the inner with twice the b value of the outer adherends [22]. However, this method does not compromise the objectives of comparing different adhesive joints and evaluating the CZM capabilities to describe the joints' behaviour. Fabrication for these joints was simpler, and a different technique, based on the use of spacers between the adherends, was used to assure t_A . Actually, the desired t_A value was achieved by supporting the top adherend of the joint (SLJ) or the two outer adherends (DLJ) with calibrated blocks in the mould during assembly to assure the correct positioning between adherends. After bonding, the joints were then left to cure in a steel mould to guarantee the lengthwise adherend alignment and value of L_0 . To guarantee the correct alignment in the testing machine, 3 mm thick and 25 mm length tabs were also bonded at the joint edges. The specimens were cured over one week at room temperature, and the excess adhesive removed by milling techniques.

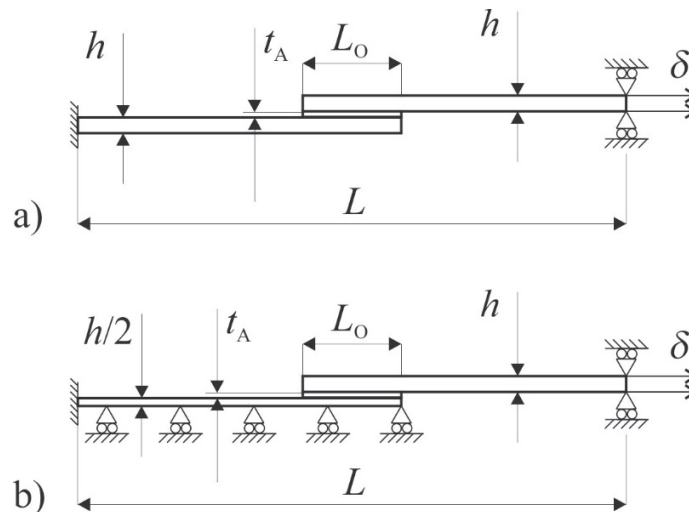


Figure 2: Geometry and dimensions of the SLJ (a) and DLJ (b).

All specimens were tested in an electro-mechanical testing machine Shimadzu AG-X 100 with a load cell of 100 kN and at a strain rate (either tensile or shear) of 0.08 s⁻¹. Fig. 3 shows the test setup for the DCB (a) and ENF specimens (b). The test setup for the SLJ and DLJ is depicted in Fig. 4.

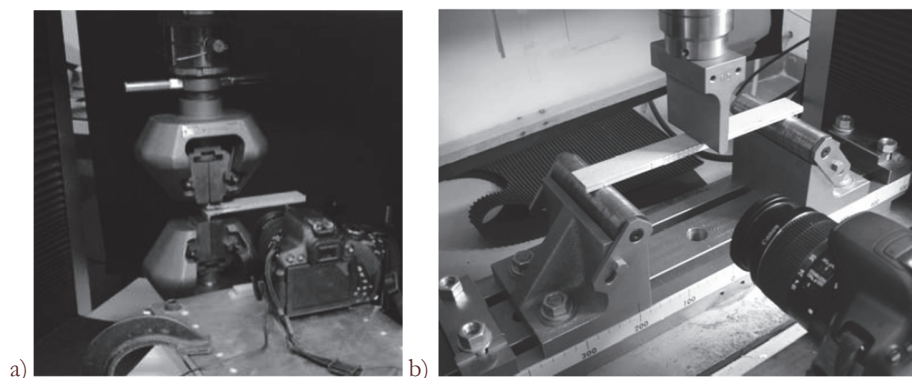


Figure 3: Test setup for the DCB (a) and ENF specimens (b).

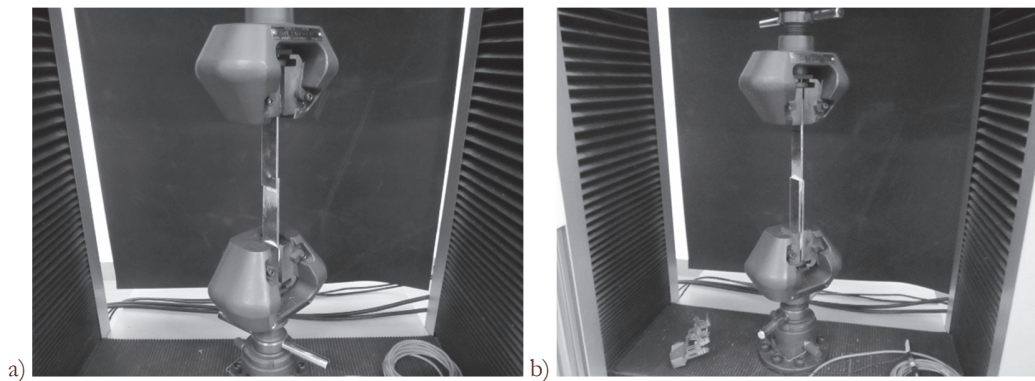


Figure 4: Test setup for the SLJ (a) and DLJ specimens (b).

The DCB, SLJ and DLJ specimens were tensile-tested using conventional grips with V-shape, to improve gripping during the test. The ENF specimens, on the other hand, were tested using a three-point bending setup, to fulfil the loading depicted in Fig. 1 (b). The fracture tests were recorded, by taking pictures with 5 s intervals, using a 18 MPixel digital camera with no zoom and fixed focal distance to approximately 100 mm. The resolution of was 0.02 mm/pixel but, in the manual measurements of a , when framing the crack tip in the printed scale, each a measurement was approximated to the nearest 1/8 of mm in the scale. The values of a resulting from this process were correlated with the P - δ curve values by the time elapsed since the beginning of each test.

Fracture toughness estimation

The conventional G_{IC} and G_{IIC} estimation methods are within the scope of Linear Elastic Fracture Mechanics (LEFM), although few methods include correction factors to account for plasticization effects (e.g. formulae proposed in the ASTM D3433-99:2005 and the BS 7991:2001 standards) [23]. As a result, these are not the most recommended for the analysis of ductile adhesive joints. In this work, G_{IC} and G_{IIC} were estimated by the DCB and ENF tests, respectively, considering the CBBM. This is a data reduction method that does not need measurements a to take place during the fracture test, since it uses an equivalent crack (a_{eq}), which is easily obtained after some manipulation from the current experimental compliance (C) which, in turn, can be found from the P - δ data (thus not involving physical measurement) [24]. The calculation of a_{eq} takes into account the fracture process zone (FPZ) acting on the crack tip in its calculation, which is neglected in methods requiring the visual a measurement. This is mandatory when measuring G_{IC} and G_{IIC} in ductile adhesives. As a result of including the FPZ, a_{eq} is higher than the measured a , by accounting for a added to the damaged zone ahead of a . The G_{IC} estimative for the DCB test by the CBBM is given as [20]

$$G_{IC} = \frac{6P^2}{B^2b} \left(\frac{2a_{eq}^2}{b^2 E_f} + \frac{1}{5G_{xy}} \right) \quad (1)$$

In this equation, a_{eq} is experimentally obtained from the current value of C , E_f is the corrected flexure modulus that includes stress concentrations effects at the crack tip, and also the stiffness variations between specimens, and G_{xy} is the adherends' shear modulus. A more detailed description of this method can be found in reference [20]. The CBBM is also available for the ENF test, and it makes possible the definition of G_{IIC} based on the current experimental C . G_{IIC} for the ENF test is calculated using the following equation

$$G_{IIC} = \frac{9P^2 a_{eq}^2}{16B^2 E_f b^3} \quad (2)$$

E_f is equivalent to that present in Eqn. (1) and, identically, it is also estimated from the experimental C . A detailed description of the derivation of Eqn. (2) is presented in reference [25].



CZM SIMULATIONS

Mixed-mode triangular model

CZM are based on relationships between stresses and relative displacements connecting homologous nodes of the cohesive elements, usually addressed as CZM laws. These laws simulate the elastic behaviour up to a peak load and subsequent softening, to model the gradual degradation of material properties up to complete failure. Under pure-mode, damage propagation occurs at a specific integration point when the stresses are released in the respective traction-separation law. Under mixed-mode, energetic criteria are often used to combine tension and shear [26]. In this work, triangular pure and mixed-mode laws, i.e. with linear softening, were considered for the analysis (Fig. 5) [27]. The elastic behaviour of the cohesive elements up to the tripping tractions is defined by an elastic constitutive matrix relating stresses and strains across the interface, containing E and G_{xy} as main parameters. Damage initiation under mixed-mode can be specified by different criteria [10]. In this work, the quadratic nominal stress criterion was considered for the initiation of damage, because of the good results found in previous works and since that damage onset is governed by adhesive stresses [16]. After the cohesive strength in mixed-mode (t_m^0) is attained, the material stiffness is degraded. Complete separation is predicted by a linear power law form of the required energies for failure in the pure-modes. For full details of the presented model, the reader can refer to reference [16].

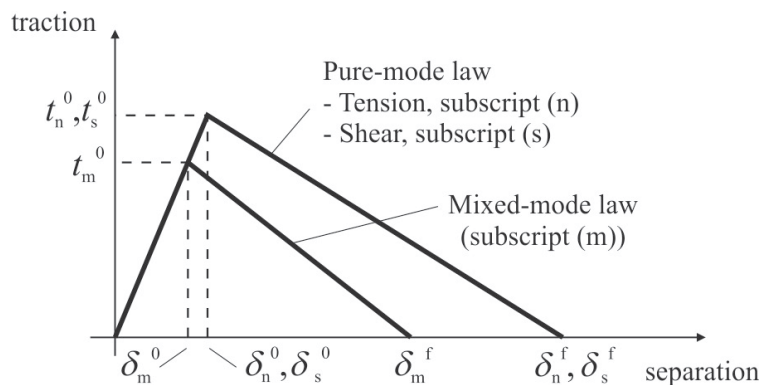


Figure 5: Traction-separation law with linear softening law available in Abaqus® (adapted from [27]).

Abaqus® implementation

The CZM simulations were run to estimate the tensile and shear CZM laws of the three adhesives by an inverse method applied to DCB and ENF specimens and, after this procedure, to validate these laws in lap geometries. In this Section, the numerical settings for both models will be described. All built models were two-dimensional (2D) and accounted for geometrical non-linearities. The stress evaluation models for the SLJ and DLJ were fully built from 4-node plane-strain elements (CPE4 from Abaqus®), and the meshes were highly refined to accurately capture the stress distributions in the adhesive layer (ten solid elements were used through-thickness in the adhesive layer). All models (DCB, ENF, SLJ and DLJ) considered a single layer of CZM elements along the bond (COH2D4 4-node cohesive elements from Abaqus®) [17] and a coarser mesh, although with a minimum refinement to assure convergence in the strength predictions (the CZM elements' size in the adhesive layer was $0.2 \text{ mm} \times 0.2 \text{ mm}$). Accuracy under identical conditions was checked in a previous work [10]. The meshes took into account size grading effects in the elements (bias effects), which depended on the type of model. These, and also boundary and loading conditions, were as follows:

- The meshes for the DCB models used bias effects to grade the elements' size in the adherends from the loading points towards the crack tip, and also vertically in the direction of the adhesive layer, where large stress gradients are expected. In the adhesive layer's length, where crack growth takes place, the mesh was built with 0.20 mm length elements to provide a smooth and accurate representation of the failure process. As boundary conditions, the lower edge node of the lower arm was fixed, and a vertical displacement and horizontal restriction was applied to the upper edge node of the upper arm.
- The adherends of the ENF specimens were modelled in the thickness direction by six elements, with a higher refinement near the adhesive and outer faces (in contact with the cylinders), thus considering double bias effects. In the specimens' length direction, the adhesive layer and cylinders' regions were modelled with a more refined mesh, considering 0.20 mm and 0.05 length elements, respectively. Horizontally, the adhesive layer's refinement

followed that of the adherends, already described. Bias effects were also equated, wherever necessary, to grade the elements' size towards the regions having higher stress gradients. The boundary conditions consisted of fixing the supporting cylinders in the joint plane and restraining the loading cylinder in the horizontal direction. The specimen was also horizontally restrained at a discrete point to prevent rigid body motion. Contact conditions were applied wherever relevant to prevent interpenetration, i.e., between all cylinders and the respective contacting faces of the specimens, and also between adherends at the initially un-bonded region.

- The SLJ and DLJ were modelled identically, apart from the consideration of the symmetry conditions applied in the DLJ, enabling to reduce the models' size. Fig. 6 shows a representative mesh for the CZM strength prediction analysis for a SLJ with $L_O=12.5$ mm. Thus, the element size at the adhesive layer's edges was $0.2 \text{ mm} \times 0.2 \text{ mm}$, and double bias effects were applied between these points. With these principles, the overlap was modelled considering between 30 and 120 elements (from $L_O=12.5$ to 50 mm). The FE mesh included edge grading horizontally from the overlap inner portion towards the overlap edges, and in the adherends vertically towards the adhesive layer, to increase the simulation speed, although keeping acceptable results. The joints were clamped at one edge and a vertical restraint and tensile displacement was applied at the opposite edge.

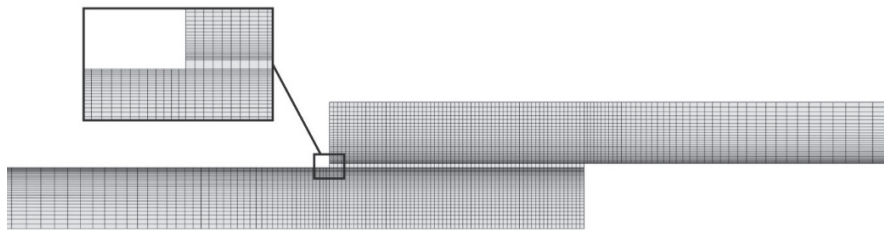


Figure 6: Mesh detail for the SLJ with $L_O=12.5$ mm.

RESULTS

Failure modes

Joint failures were cohesive in the adhesive layer. For all the joints bonded with the Araldite® AV138, the type of failure was also cohesive, but near the interface. Moreover, as explained further, some failures were accompanied by plasticization of the adherends. Fig. 7 presents example failure modes for SLJ bonded with the Araldite® 2015.

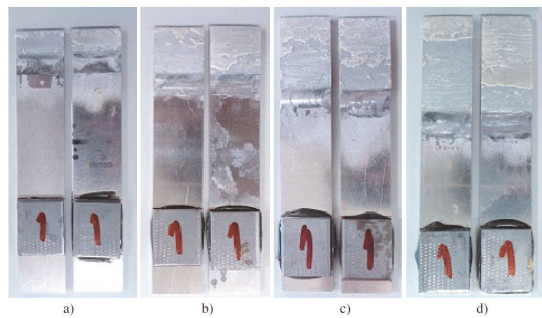


Figure 7: Example of cohesive failures for the SLJ bonded with the Araldite® 2015 and $L_O=12.5$ (a), 25 (b), 37.5 (c) and 50 mm (d).

Tensile and shear CZM laws

The CZM laws' estimation was divided into the G_{IC} and G_{IIC} calculation by the previously described CBBM, which is an entirely experimental procedure, and the numerical inverse data fitting procedure leading to the full CZM definition.

G_{IC} and G_{IIC} calculation

The initial stage of the inverse procedure to estimate the tensile and shear CZM laws is the definition of G_{IC} and G_{IIC} by the DCB and ENF tests, respectively. Data reduction was accomplished by the previously described CBBM. The $P-\delta$ curves of the DCB and ENF experiments were the basis for this analysis and, overall, these revealed a close tendency for each test type/adhesive set. It should be mentioned that the DCB and ENF $P-\delta$ curves for some specimens bonded with the Araldite®

AV138 intercalated regions of progressive crack growth with others showing unstable crack growth, which occurred due to the brittle characteristics of this adhesive. On the other hand, all joints bonded with the Araldite® 2015 and Sikaforce® 7752 fractured in a more gradual manner, which also reflected on the smooth evolution of P during crack propagation. The R-curves, which represent G_I or G_{II} vs. a , all showed crack propagation with a steady value of G_I or G_{II} (except for the aforementioned brittle failure phenomena). Fig. 8 presents example R-curves for the DCB (a) and ENF specimens (b) (one curve for each adhesive).

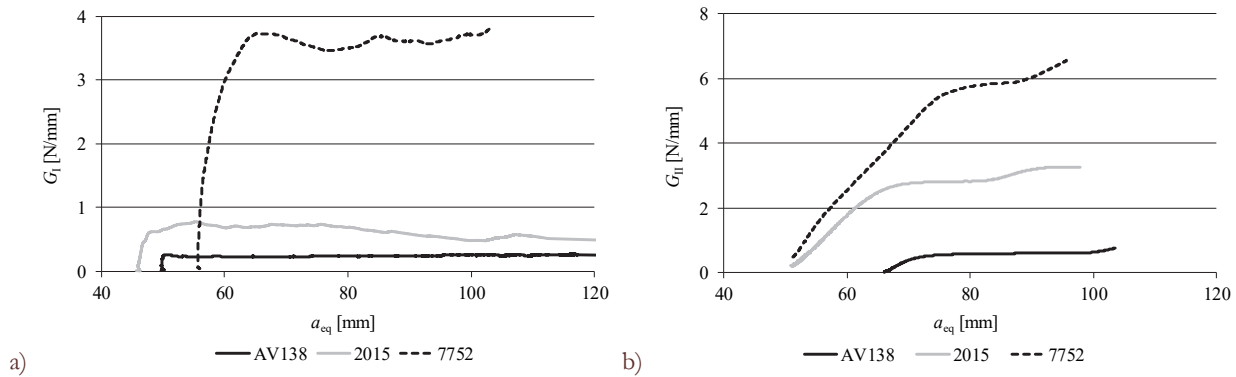


Figure 8: Example R-curves for the DCB (a) and ENF specimens (b).

These values were then defined as G_{IC} and G_{IIC} , respectively [28]. Ideally, the R-curves are perfectly horizontal during crack propagation, because this stage theoretically occurs at a constant G_I or G_{II} . However, in practice, oscillations are observed owing to experimental issues such as different adhesive mixing, poor adhesion, voids, defects and crack arrest [29]. In the ENF test, the G_{IIC} measurement region spans from the undamaged state until close to the loading cylinder. Here, the applied loading puts the crack under additional compression, thus cancelling the pure shear loading required to measure G_{IIC} , which therefore renders the G_{IIC} measurements not valid.

Adhesive Specimen	Araldite® AV138		Araldite® 2015		Sikaforce® 7752	
	G_{IC}	G_{IIC}	G_{IC}	G_{IIC}	G_{IC}	G_{IIC}
1	0.231	0.572	0.444	2.545	3.420	5.863
2	0.247	0.712	0.467	2.943	3.900	5.886
3	0.234	0.594	0.492	2.801	3.840	5.470
4	0.310	0.562	0.460	3.136	4.000	4.811
5	0.254	0.576	0.709	2.901	3.400	5.681
6	0.217	0.585	0.663	3.025	3.650	5.656
Average	0.249	0.600	0.539	2.892	3.702	5.561
Standard deviation	0.033	0.056	0.116	0.204	0.253	0.398

Table 2: Average values of G_{IC} and G_{IIC} and respective standard deviation [in N/mm] obtained by the DCB and ENF tests, respectively.

The obtained G_{IC} and G_{IIC} (N/mm) CBBM data is presented in Tab. 2 for both DCB and ENF tests and all adhesives. The results showed a small scatter between each test type/adhesive set, i.e., each column set of data. The percentile standard deviations were mostly under 10%, although the highest scatter found was for the G_{IC} test and Araldite® 2015, equal to 21.5%. A comparison can be made between the fracture data of Tab. 2 with that of Tab. 1, obtained from literature results. Some deviations are found, although the values are in the same order of magnitude. This offset is attributed to differences in the restraint effects to the adhesive layer (b and t_A), which affects the fracture properties by inducing modifications of the FPZ size around the crack tip [30].

Inverse CZM law estimation

The inverse technique applied to the DCB and ENF specimens was undertaken here, as described in the Methodology Section, taking as basis the fracture information gathered, namely the G_{IC} and G_{IIC} values depicted in Tab. 2. For all adhesives

and test methods, individual models were considered with the same dimensions of the respective experimental test and the obtained G_{IC} or G_{IIC} . To achieve the goal of having the same dimensions in the DCB and ENF numerical models and real specimens, the values of B , t_A and b were measured in the real specimens with a digital micrometre having a resolution of 1 μm . The values of a_0 were measured with a digital calliper with a resolution of 10 μm . After, these dimensions were considered to construct individual numerical models for each specimen. E and G_{xy} were fixed from the data of Tab. 1. t_n^0 and t_s^0 were parameters to define and enable the full definition of the CZM laws. Initially, these parameters were set as equal to σ_f and ultimate shear strength (τ_f), respectively, also depicted in Tab. 1.

Tensile CZM law

The tensile CZM laws of the adhesives were defined by an inverse procedure applied to the P - δ curves of the respective DCB tests. During the inverse process, it was found that t_n^0 has a negligible effect on the outcome of the P - δ curves, only with minor stiffness variations near the peak load (corresponding to the onset of crack growth) and corresponding peak load changes. This agrees with a previous work on composite DCB bonded joints [19]. The behaviour during crack growth is unaffected by modifications of this parameter. As a result, and since G_{IC} was estimated individually for each specimen, the initial set of CZM parameters led to a good representation of the experimental behaviour. Fig. 9 gives an example of P - δ curves comparison for a DCB specimen bonded with the Araldite® AV138. This specimen gives a good representation of the level of agreement found for this adhesive, in which the numerical simulations managed to reproduce satisfactorily the experimental data. Compared to the experiments, and due to non-existence of experimental effects that led to some instabilities, the P evolution during crack growth was highly stable. The results were equally good for the Araldite® 2015 but, for the Sikaforce® 7752, the loads during crack growth were slightly under the experiments. The analysis showed that this was due to modelling a highly ductile adhesive with a triangular CZM, which leads to a depreciation of the transmitted stresses when the adhesive initiates damage.

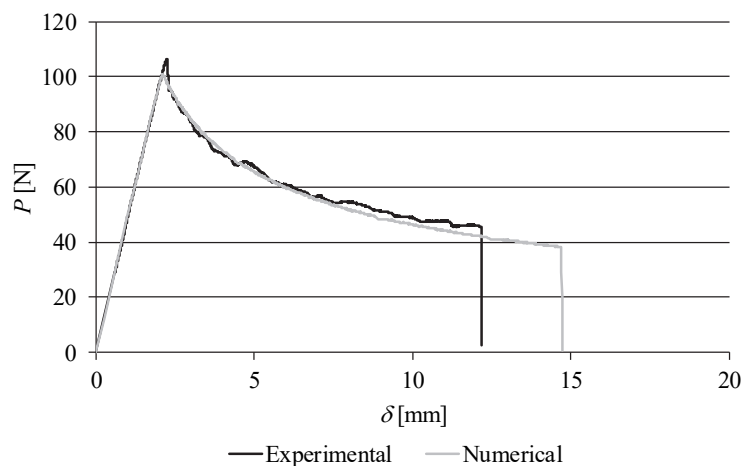


Figure 9: Example of P - δ curves comparison for a DCB specimen bonded with the Araldite® AV138.

Fig. 10 presents the tensile CZM law results of the three adhesives, after the fitting process. For each of the adhesives, an average CZM law is also included, which is calculated based on the average t_n^0 and G_{IC} of all specimens. The t_n^0 values are identical within each adhesive, following the aforementioned discussion on the almost nil influence of this parameter, whilst some deviations were found in δ_n^f , arising from the G_{IC} variations between specimens. Nonetheless, it can be considered that there is a good repeatability for the three adhesives. The average values and deviation (percentile deviations in parentheses) of δ_n^f were as follows: 0.0156 ± 0.0014 mm (9%) for the Araldite® AV138, 0.055 ± 0.011 mm (22%) for the Araldite® 2015 and 0.719 ± 0.061 mm (8%) for the Sikaforce® 7752. These values are in agreement with the known increasing ductility of these three adhesives from the Araldite® AV138 to the Sikaforce® 7752.

Shear CZM law

A similar inverse analysis was undertaken for the ENF specimens, to estimate the shear CZM laws of the three adhesives. This procedure showed that, oppositely to the DCB specimens, t_s^0 has a major effect on the fitting process, and its adjustment is required such that a good correspondence is found between the experiments and simulations. More



specifically, higher t_s^0 increases the peak load at crack initiation and the stiffness up to that point in the P - δ curve, and it also induces a more abrupt post-peak load reduction during the crack growth stage. Azevedo et al. [14], in a previous work, found an identical tendency in the inverse analysis of ENF bonded joints with aluminium alloy adherends. Because of this, it was necessary to undertake an iterative process of changing t_s^0 until finding the best match between the tests and simulations. Fig. 11 shows an example of end result of this process for an ENF specimen bonded with the Araldite® 2015. In the particular case of the ENF specimen, it was possible to define a t_s^0 value, even for the highly ductile Sikaforce® 7752, that could closely match the experimental respective P - δ curve. However, this may be due to the expense of artificially increasing t_s^0 over the correct value, as it will be checked in the validation stage of this work.

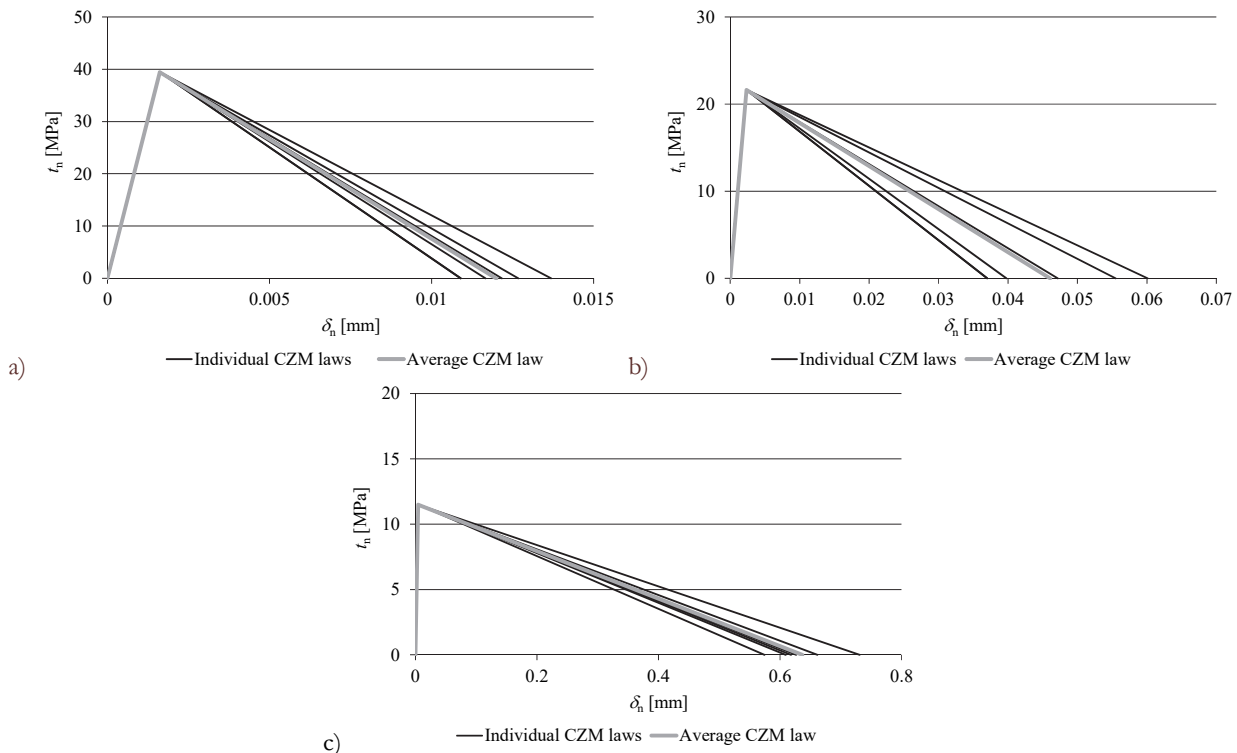


Figure 10: Estimated tensile CZM laws for the Araldite® AV138 (a), Araldite® 2015 (b) and Sikaforce® 7752 (c).

The full set of shear CZM laws obtained by this process can be found in Fig. 12, after the inverse process is completed. The average law is superimposed to the fitted laws (estimated from the average t_s^0 and G_{IIC} of all specimens). Here, some scatter was found for t_s^0 , which was necessary to have a good match for all specimens. Despite these differences, and also the G_{IIC} variations (depicted in Tab. 2), the shear CZM laws have a similar behaviour within each adhesive type. The t_s^0 averages and deviations (including the percentile deviations in parentheses) were: 19.85 ± 3.22 MPa (16%) for the Araldite® AV138, 19.21 ± 1.65 MPa (9%) for the Araldite® 2015 and 19.5 ± 2.06 MPa (11%) for the Sikaforce® 7752. The same analysis follows for δ_s^f : 0.0645 ± 0.0094 mm (15%) for the Araldite® AV138, 0.316 ± 0.049 mm (16%) for the Araldite® 2015 and 0.588 ± 0.092 mm (16%) for the Sikaforce® 7752. Equally to the DCB results, the variations of δ_s^f reflect the differences in ductility between the three adhesives.

Joint stress analysis

A comparison between σ_y and τ_{xy} stress distributions of the SLJ and DLJ is presented in this Section, to serve as basis for the joint strength evaluation that follows. Fig. 13 and Fig. 14 show σ_y and τ_{xy} stress distributions at the adhesive mid-thickness as a function of x/L_0 ($0 \leq x \leq L_0$), respectively, for the SLJ (a) and DLJ (b) bonded with the Araldite® 2015. Despite the stresses of the other two adhesives are not presented, they are in fact similar, yet small variations were found due to the different adhesives' stiffness used in this work (higher stiffness moderately increases peak stresses at the overlap ends [31]). Both σ_y and τ_{xy} stresses are normalized by τ_{avg} , hence representing the average value of τ_{xy} in the adhesive bond for each value of L_0 . Moreover, these stresses were assessed during the elastic phase, which makes them valid until the onset of adherend or adhesive plasticization.

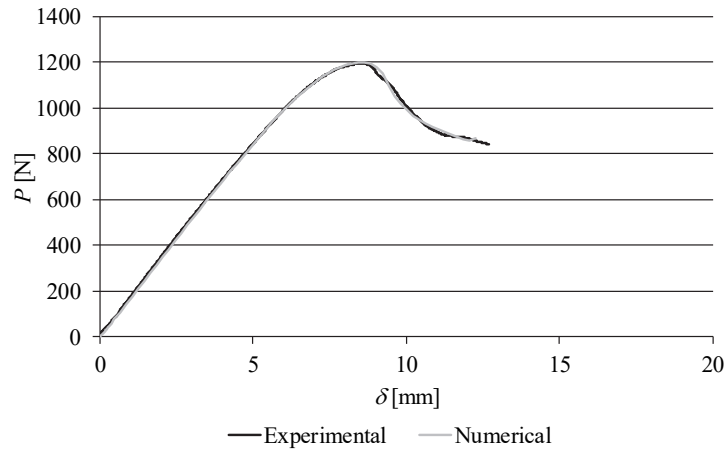


Figure 11: Example of P- δ curves comparison for an ENF specimen bonded with the Araldite® 2015.

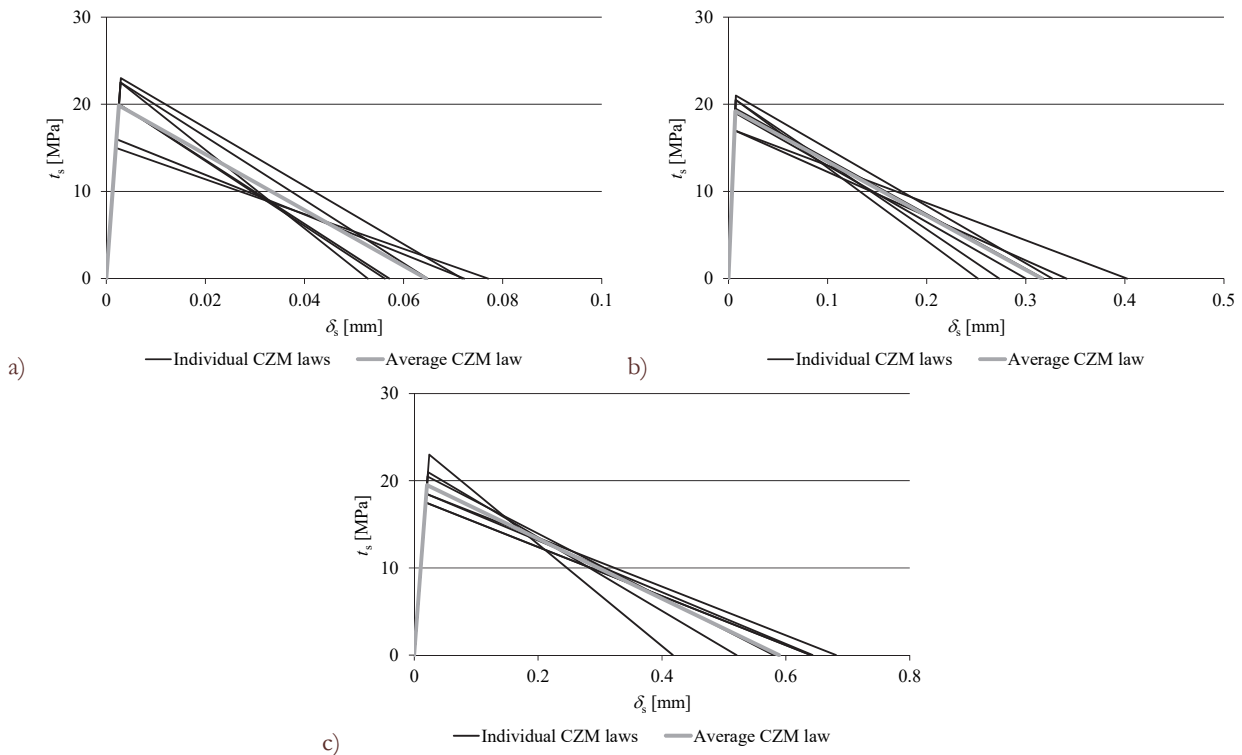


Figure 12: Estimated shear CZM laws for the Araldite® AV138 (a), Araldite® 2015 (b) and Sikaforce® 7752 (c).

Fig. 13 (a) depicts σ_y stresses for the SLJ across the overlap, which are commonly smaller in magnitude than τ_{avg} . Nevertheless, higher σ_y peak stresses can be found at the overlap ends due to the adherends rotation that induces their separation at the overlap edges and compression in-between [32]. Evaluating the evolution of the normalized σ_y stresses, one can conclude that the peak values increase with L_O . This behaviour is responsible for a significant P_m reduction of the bonded joints, constituting one of the main factors for damage initiation at the overlap edges, particularly for joints bonded with brittle adhesives [33]. The DLJ design is skilled to reduce the bending moment due to the symmetry of the applied loads [34]. Fig. 13 (b), related to σ_y stresses for the DLJ, shows an identical behaviour to that of SLJ at $x/L_O=0$, yet with lower magnitude [35]. σ_y stresses are close to nil at the centre of the overlap, although presenting higher gradients in the direction of the ends of the overlap with increasing L_O . On the other hand, compressive peaks are found at $x/L_O=1$.

Thus, stresses for DLJ have an improved efficiency over SLJ and, as a result, P_m should over-double P_m of the SLJ for the same L_O .

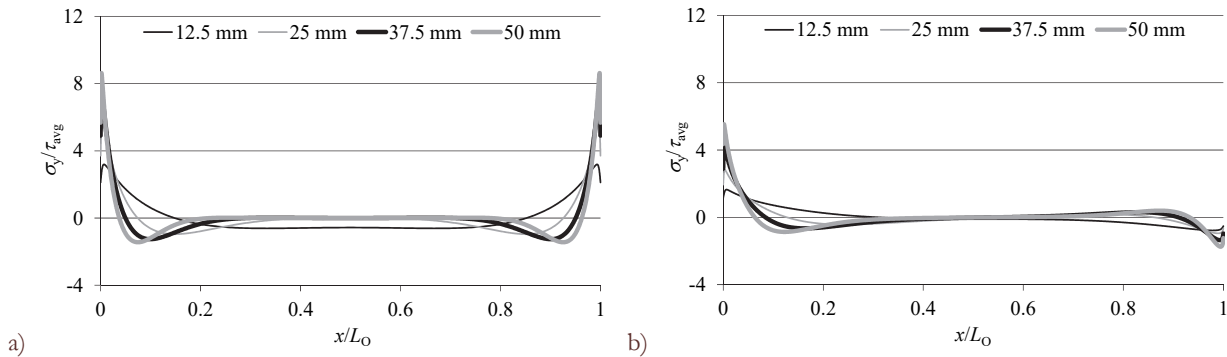


Figure 13: σ_y stress distributions at the adhesive mid-thickness as a function of L_O for the SLJ (a) and DLJ (b).

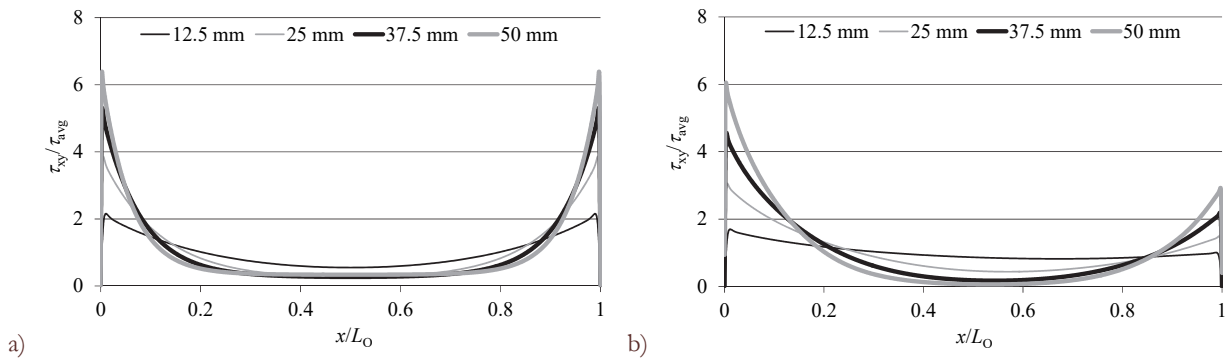


Figure 14: τ_{xy} stress distributions at the adhesive mid-thickness as a function of L_O for the SLJ (a) and DLJ (b).

Fig. 14 (a) shows the obtained τ_{xy} stress profiles for the SLJ, in which τ_{xy} stresses peak at the overlap edges, and present smaller values at the overlap inner region [36, 37]. This is caused by the adherends' differential deformation along the overlap. Indeed, the adherends are increasingly loaded from their free overlap edge towards the other overlap edge. τ_{xy} peak stresses increase with L_O mainly due to the growing variations of adherend longitudinal strains as L_O becomes larger [16]. This is detrimental for the joint behaviour especially when using brittle adhesives [38]. Actually, the overall strength is affected by the smaller allowable plastic deformation that the adhesive can endure, and the strength improvement with L_O should be reduced. While brittle adhesives fail upon the attainment of the adhesive strength at the overlap ends, the ductile ones allow plasticization, putting the adhesive layer under load when the adhesive at the overlap ends starts to yield [39]. Therefore, ductile adhesives have a significant P_m improvement with L_O . The τ_{xy} stress distributions for the SLJ depicted in Fig. 14 (b) show a higher peak at the outer overlap end than the opposed one due to the higher loads carried by the middle adherend. Comparing with the SLJ design, τ_{xy} stresses diminish at the inner overlap end due to the reduced variation between the exterior and interior adherends' longitudinal deformations, thus reducing the differential straining effect. Moreover, τ_{xy} stresses for the DLJ at the both overlap ends are considerably smaller in normalized magnitude, which will benefit P_m and, probably, more than the double of the SLJ strength should be attained [40]. Additionally, and similarly to the SLJ, P_m should not increase proportionally with L_O , because σ_y peel and τ_{xy} peak stresses at the overlap edges increase with L_O .

Experimental joint strengths

Fig. 15 depicts the P_m average experimental values and respective deviation for the SLJ (a) and DLJ (b) bonded with the three adhesives. At first glance, P_m highly depends on the used adhesive. Regarding the SLJ evaluation (Fig. 15 a), the P_m increase with L_O for the adhesive Araldite® AV138 is not so pronounced as for the others adhesives. For $L_O=12.5$ mm, P_m is very similar for the two Araldite® adhesives (≈ 5.3 kN), and the Sikaforce® 7752 is lower than the AV138 by 33.1%. The

Araldite® 2015 accomplishes higher performance for $L_O=25$ mm (≈ 9.5 kN), attaining an increase of 79.3% comparing with the lowest L_O . Indeed, at this L_O , the Araldite® 2015 P_m exceeds the other two adhesives by 28.9% (Araldite® AV138) and 24.3% (Sikaforce® 7752). For $L_O=37.5$ mm, the Araldite® 2015 still has the highest P_m (≈ 12.2 kN), while the Sikaforce® 7752 is lower by 13.5%, and the Araldite® AV138 by 52.6%. Regarding $L_O=50$ mm, P_m for the Araldite® 2015 and Sikaforce® 7752 attained ≈ 15.2 and ≈ 14.4 kN, respectively. P_m for the Araldite® AV138 is lower by 62.5 and 53.9% compared to the Araldite® 2015 and Sikaforce® 7752, respectively. The maximum values of percentile standard deviation were 8.1% for Araldite® AV138, 4.4% for Araldite® 2015 and 6.2% for Sikaforce® 7752.

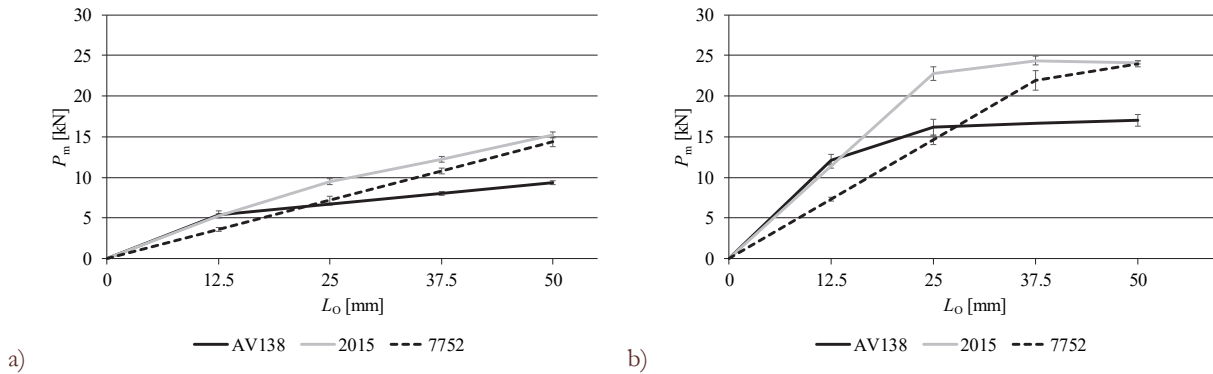


Figure 15: Experimental P_m for the SLJ (a) and DLJ (b) bonded with the three adhesives.

The P_m evaluation for the DLJ (Fig. 15 (b)) showed that, for $L_O=12.5$ mm, the Araldite® AV138 and Araldite® 2015 provide the best results, of ≈ 12 kN, with slight advantage for the Araldite® AV138. The relative deviation of the Sikaforce® 7752, when compared with the other two adhesives, was -66.9 and -56.7% for the Araldite® AV138 and Araldite® 2015, respectively. For $L_O=25$ mm, the Araldite® 2015 outperforms the other adhesives with P_m of ≈ 22.7 kN, attaining a difference of 29.1 and 35.6% for the Araldite® AV138 and the Sikaforce® 7752, respectively. For $L_O \geq 25$ mm, the P_m evolution for the adhesive Araldite® AV138 is practically nil, and it remains close to 16 kN. For $L_O=37.5$ mm, P_m for the Araldite® 2015 and the Sikaforce® 7752 tends to become similar, at ≈ 24 and ≈ 22 kN, respectively, while the Araldite® AV138 presents only 16.6 kN. The percentile difference between this adhesive with respect to the Sikaforce® 7752 and Araldite® 2015 was -31.2 and -46.1%, respectively. Regarding $L_O=50$ mm, both Araldite® 2015 and the Sikaforce® 7752 behaved similarly ($P_m \approx 24$ kN), while the Araldite® AV138 showed an average of 16.9 kN. Thus, the difference of the Araldite® 2015 is 0.5% to the Sikaforce® 7752 and 42.0% to the Araldite® AV138. It should be noted that the strength of the DLJ tested with the Araldite® 2015 adhesive ($L_O=25, 37.5$ mm and 50 mm) and Sikaforce® 7752 ($L_O=37.5$ and 50 mm) is limited by the adherends' yielding. Due to the adherends' plasticization, none of the adhesives presents a total proportionality of P_m as a function of L_O . Actually, while the Araldite® AV138 does not have proportionality at all, the Araldite® 2015 has it up to $L_O=25$ mm, while Sikaforce® 7752 records proportionality up to $L_O=37.5$ mm. The maximum values of percentile standard deviation were 6.1% for Araldite® AV138, 3.6% for Araldite® 2015 and 5.5% for Sikaforce® 7752. Similar to the SLJ, the highest P_m variation between L_O limit values also occur in the joints tested with the Sikaforce® 7752, given its high ductility. On the other hand, the lower P_m variation is again attributed to the Araldite® AV138. This is due to its inherent reduced plasticization capacity of the adhesive, due to its brittleness, which implies the joint failure as soon as the limiting stresses are reached at the overlap ends.

Comparing the SLJ and DLJ bonded with the Araldite® AV138, a more than two times P_m improvement was found, except for $L_O=50$ mm. Indeed, P_m increases by 123.9, 139.2 and 107.9% for $L_O=12.5, 25$ and 37.5 mm, respectively. For the larger L_O the P_m increase was by 81.7%, due to the adherend plasticization effects. Comparing SLJ with DLJ bonded with the Araldite® 2015, P_m increases by 115.7, 139.8, 99.0 and 58.7% with $L_O=12.5, 25, 37.5$ and 50 mm, in the same order. Comparing the SLJ and DLJ for the Sikaforce® 7752, P_m increases by 100.7, 103.8, 103.0 and 66.7%, for $L_O=12.5, 25, 37.5$ and 50 mm, respectively.

CZM law validation

This Section provides a comparative evaluation between the experimental and numerical results for the three adhesives with both SLJ and DLJ geometries. The numerical analyses were performed as described, whilst the work methodology and inverse CZM law estimation, which are on the basis of this analysis, were also previously described. Initially, Fig. 16 and Fig. 17 present the stiffness degradation (SDEG variable), attained at P_m , of the CZM elements representing the adhesive layer for the SLJ and DLJ, respectively. In these figures, the Araldite® AV138 (a) and Sikaforce® 7752 (b) were considered

as example adhesives. The SDEG variable ranges from 0 (no damage in the CZM law) to 1 (full damage in the CZM law). First, it can be found that damage in the SLJ is symmetric, which agrees with the stress distributions depicted in Fig. 13 (a) and Fig. 14 (a), and shows that cracking initiated simultaneously at both overlap edges. In the DLJ, damage accumulates at the overlap edge in which peak stresses concentrate (Fig. 13 (b) and Fig. 14 (b)). As a result, cracking initiates also at this edge. Between adhesives, more flexible adhesives such as the Sikaforce® 7752 attain P_m with smaller absolute SDEG values, which can be attested by the lighter grey colour in the adhesive, and is justified by the smoother stress plots for this adhesive (Fig. 13 and Fig. 14).

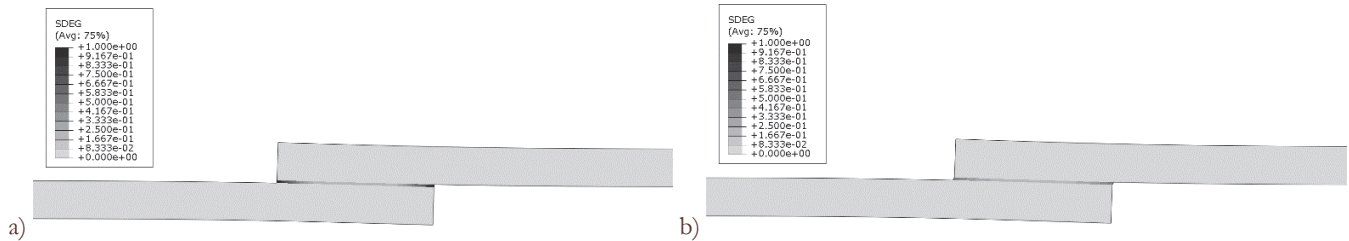


Figure 16: SDEG variable at P_m for the SLJ bonded with the Araldite® AV138 (a) and Sikaforce® 7752 (b).

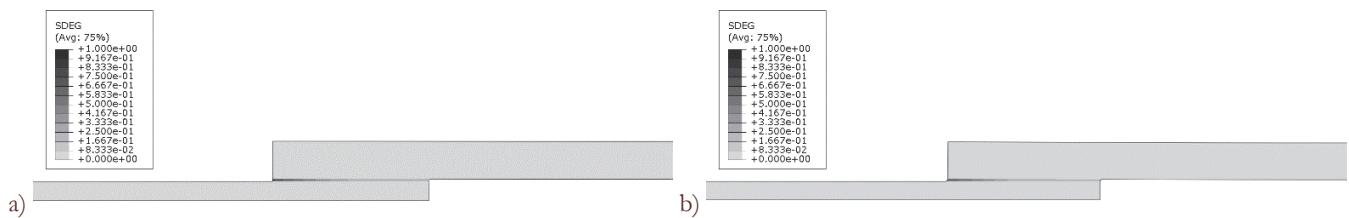


Figure 17: SDEG variable at P_m for the DLJ bonded with the Araldite® AV138 (a) and Sikaforce® 7752 (b).

Fig. 18 depicts a good correlation on the experimental/numerical P_m comparison for the joints bonded with the Araldite® AV138. Actually, the maximum relative deviation for the SLJ was -5.82%, found for $L_o=12.5$ mm. Moreover, the data shows relative deviations of -2.8, -1.0 and 0.5% found for $L_o=25, 37.5$ and 50 mm, respectively. For the DLJ, the maximum relative deviation was -4.2%, found for $L_o=12.5$ mm. For the other configurations, the obtained differences were 3.4% ($L_o=25$ mm), 1.3% ($L_o=37.5$ mm) and 0.2% ($L_o=50$ mm). Here, the CZM models managed to capture the cohesive failure of the adhesive without adherends' plasticization for the SLJ, and also the plasticization effect that was found for the DLJ with $L_o \geq 25$ mm, and that proved to highly affect failure of this non-plasticizing adhesive.

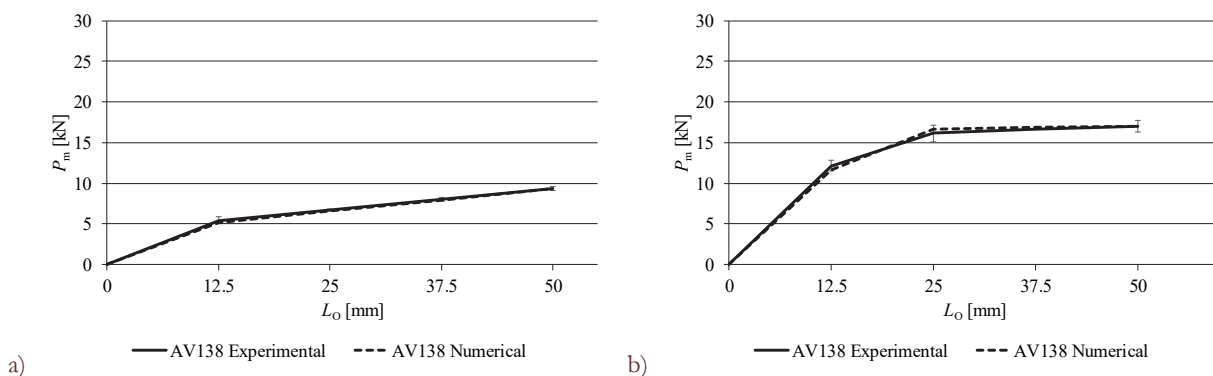


Figure 18: Experimental and CZM P_m comparison for the SLJ (a) and DLJ (b) bonded with the Araldite® AV138.

Fig. 19, related to the Araldite® 2015, also presents a good correlation between the experiments and numerical data. In fact, the maximum relative deviation for the SLJ was about 5.2%, corresponding to $L_o=37.5$ mm. With respect to the other L_o values, the relative deviations were 4.2, 3.2 and 4.2%, for $L_o=12.5, 25$ and 50 mm, respectively. The DLJ with this adhesive gave the best match to the experimental tests between all adhesives and joint types. The maximum relative deviations were 0.2, 0.9, 2.2 and 3.6%, found for increasing L_o between 12.5 and 50 mm. In this case, the adherends' yielding effect was noted by a smaller extent for the DLJ with $L_o=25$ mm, due to the higher attained P_m compared to the joints bonded with



the Araldite® AV138, and to a higher extent for the DLJ with $L_O=37.5$ and 50 mm. Also in these joints, the models managed to capture the experimental failure.

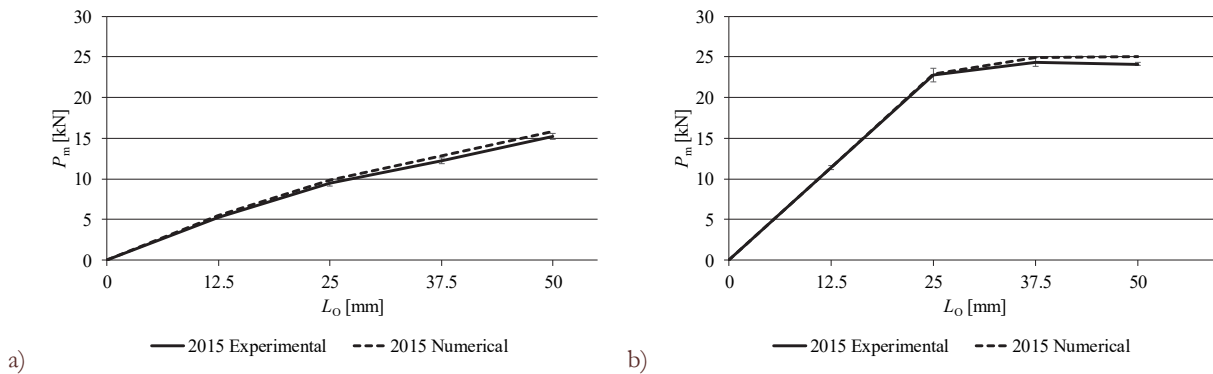


Figure 19: Experimental and CZM P_m comparison for the SLJ (a) and DLJ (b) bonded with the Araldite® 2015.

The Sikaforce® 7752 results can be found in Fig. 20. For these conditions, large deviations exist between the two data sets, for both SLJ and DLJ, with the numerical results showing higher P_m than the experimental average P_m . Through a detailed analysis of the numerical simulations, it was concluded that this difference was due to the excess estimation of t_s^0 for this adhesive in particular. In fact, due to the use of a triangular cohesive law to model a high ductility adhesive, it was necessary to increase t_s^0 in the inverse adjustment process of the ENF results, respectively. Thus, the subsequent application of these values for the strength prediction of adhesive joints leads to the excess estimation of P_m . For the SLJ, the lowest deviation was 38.71% ($L_O=12.5$ mm). For $L_O=25, 37.5$ and 50 mm, the relative deviations were 46.43, 48.17 and 50.78%, in this order. The DLJ also showed high deviations between numerical and experimental data. The minimum relative deviation was 49.7%, found for $L_O=12.5$ mm. On the other hand, deviations of 57.9, 14.1 and 4.1% were found for $L_O=25, 37.5$ and 50 mm, respectively.

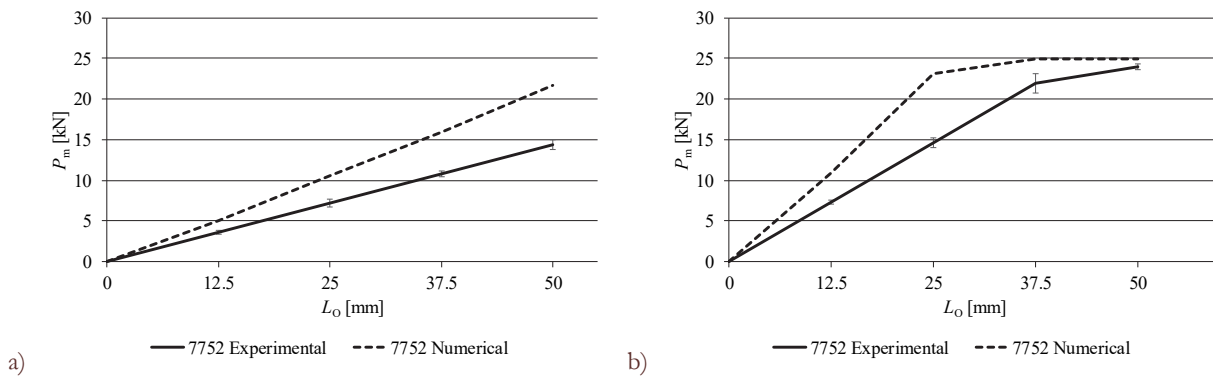


Figure 20: Experimental and CZM P_m comparison for the SLJ (a) and DLJ (b) bonded with the Sikaforce® 7752.

CONCLUSIONS

This work aimed at estimating the tensile and shear CZM laws of three structural adhesives by an inverse technique applied to DCB and ENF fracture tests, respectively, to enable their further use in the strength prediction of bonded joints with arbitrary geometry and loading. With this purpose, validation was undertaken with experimental SLJ and DLJ results. Application of the inverse technique initiated by the experimental estimation of G_{IC} and G_{IIC} by the fracture tests, whose $P-\delta$ curves showed a good agreement for each test type/adhesive set. Few unstable crack growth phenomena were observed for the Araldite® AV138, due to its brittleness. The resulting R -curves showed crack growth with a steady value of G_I or G_{II} , which enabled calculation of G_{IC} and G_{IIC} . The fitting process for the DCB specimens showed that t_n^0 has a negligible influence on the outcome of the $P-\delta$ curves and, as a result, the initial values provided a good response. On the other hand, this did not occur for the ENF specimens, in which the adjustment of t_s^0 was clearly a necessity to adjust the curves. Validation of the CZM laws followed with SLJ and DLJ bonded with the same adhesives. The experimental



behaviour of the joints was highly dependent on the adhesive type and L_0 , and this was conveniently explained by a stress analysis. The brittle Araldite® AV138 was only competitive for short L_0 due to high peak stresses, whilst less strong but more ductile adhesives gradually gain ground by increasing L_0 due to their plasticization ability. The DLJ showed a significantly improved behaviour over the SLJ, although these were affected by adherends' yielding, which limited P_m for some joint configurations. The validation process showed accurate P_m predictions for the Araldite® AV138 and 2015, whilst the P_m predictions for the Sikaforce® 7752 overshot the experimental results. A detailed analysis revealed that this was due to using a triangular CZM law, which in this case is not the most adequate. As a main conclusion, the inverse CZM parameter identification showed to be a valid and accurate technique for not too ductile adhesives, for which a different CZM law shape could provide a good solution.

ACKNOWLEDGMENTS

The authors would like to thank Sika® Portugal for supplying the adhesive.

REFERENCES

- [1] Petrie, E.W. (1999). Handbook of adhesives and sealants. 2nd ed ed. New York: McGraw-Hill.
- [2] Brockmann, W., Geiß, P.L., Klingen, J., Schröder, K.B., Mikhail, B. (2008). Adhesive Bonding: Materials, Applications and Technology: Wiley.
- [3] da Silva, J.F.M.G., Öchsner, A., Adams, R.D. (2011). Handbook of Adhesion Technology. Heidelberg: Springer.
- [4] Adams, R.D. (2005). Adhesive Bonding, Science, technology and applications. Cambridge England: Woodhead Publishing.
- [5] Ávila, A.F., Bueno, P.n.d.O. (2004). Stress analysis on a wavy-lap bonded joint for composites. *International Journal of Adhesion and Adhesives*.24, pp. 407-414. DOI: 10.1016/j.ijadhadh.2003.12.001.
- [6] Volkersen, O. (1938). Die nietkrafteerteilung in zubeanspruchten nietverbindungen konstanten loschonquerschnitten. *Luftfahrtforschung*.15 pp. 41-47.
- [7] Barenblatt, G.I. (1959). The formation of equilibrium cracks during brittle fracture. General ideas and hypotheses. Axially-symmetric cracks. *Journal of Applied Mathematics and Mechanics*.23, pp. 622-636. DOI: 10.1016/0021-8928(59)90157-1.
- [8] Dugdale, D.S. (1960). Yielding of steel sheets containing slits. *J Mech Phys Solids*.8, pp. 100-4. DOI: 10.1016/0022-5096(60)90013-2.
- [9] da Silva, L.F.M., Campilho, R.D.S.G. (2012). Advances in Numerical Modelling of Adhesive Joints. *Advances in Numerical Modeling of Adhesive Joints: Springer Berlin Heidelberg*, pp. 1-93.
- [10] Rocha, R.J.B., Campilho, R.D.S.G. (2018). Evaluation of different modelling conditions in the cohesive zone analysis of single-lap bonded joints. *J Adhesion* 94, pp. 562-582. DOI: 10.1080/00218464.2017.1307107.
- [11] Pandya, K.C., Williams, J.G. (2000). Measurement of cohesive zone parameters in tough polyethylene. *Polymer Engineering & Science* 40, pp. 1765-1776. DOI: 10.1002/pen.11308.
- [12] da Silva, L.F.M., Campilho, R.D.S.G. (2012). Advances in numerical modelling of adhesive joints. Heidelberg: Springer.
- [13] Xu, Y., Guo, Y., Liang, L., Liu, Y., Wang, X. (2017). A unified cohesive zone model for simulating adhesive failure of composite structures and its parameter identification. *Composite Structures*.182, pp. 555-565. DOI: 10.1016/j.compstruct.2017.09.012.
- [14] Azevedo, J.C.S., Campilho, R.D.S.G., da Silva, J.F.G., Faneco, T.M.S., Lopes, R.M. (2015). Cohesive law estimation of adhesive joints in mode II condition. *Theor Appl Fract Mec*.80, pp. 143-154.
- [15] Bouhala, L., Makradi, A., Belouettar, S., Younes, A., Natarajan, S. (2015). An XFEM/CZM based inverse method for identification of composite failure parameters. *Computers & Structures*.153, pp. 91-97. DOI: 10.1016/j.compstruc.2015.02.035.
- [16] Campilho, R.D.S.G., Banea, M.D., Pinto, A.M.G., da Silva, L.F.M., de Jesus, A.M.P. (2011). Strength prediction of single- and double-lap joints by standard and extended finite element modelling. *Int J Adhes Adhes*. 31, pp. 363-372. DOI: 10.1016/j.ijadhadh.2010.09.008.



- [17] Campilho, R.D.S.G., Banea, M.D., Neto, J.A.B.P., da Silva, L.F.M. (2013). Modelling adhesive joints with cohesive zone models: effect of the cohesive law shape of the adhesive layer. *Int J Adhes Adhes.* 44, pp. 48-56. DOI: 10.1016/j.ijadhadh.2013.02.006.
- [18] Faneco, T., Campilho, R., Silva, F., Lopes, R. (2017). Strength and Fracture Characterization of a Novel Polyurethane Adhesive for the Automotive Industry. *J Test Eval.* 45, pp. 398-407. DOI: 10.1520/JTE20150335.
- [19] Fernandes, R.L., Campilho, R.D.S.G. (2017). Testing different cohesive law shapes to predict damage growth in bonded joints loaded in pure tension. *J Adhesion.* 93, pp. 57-76. DOI: 10.1080/00218464.2016.1169176.
- [20] Constante, C.J., Campilho, R.D.S.G., Moura, D.C. (2015). Tensile fracture characterization of adhesive joints by standard and optical techniques. *Eng Fract Mech.* 136, pp. 292-304. DOI: 10.1016/j.engfracmech.2015.02.010.
- [21] Leitão, A.C.C., Campilho, R.D.S.G., Moura, D.C. (2016). Shear Characterization of Adhesive Layers by Advanced Optical Techniques. *Exp Mech.* 56, pp. 493-506. DOI: 10.1007/s11340-015-0111-4.
- [22] Markolefas, S.I., Papathanassiou, T.K. (2009). Stress redistributions in adhesively bonded double-lap joints, with elastic–perfectly plastic adhesive behavior, subjected to axial lap-shear cyclic loading. *Int J Adhes Adhes.* 29, pp. 737-744. DOI: 10.1016/j.ijadhadh.2009.04.001.
- [23] Giovanola, J.H., Finnie, I. (1984). A review of the use of the J integral as a fracture parameter. *Solid Mechanics Archives.* 9, pp. 197-225.
- [24] de Moura, M.F.S.F., Campilho, R.D.S.G., Gonçalves, J.P.M. (2008). Crack equivalent concept applied to the fracture characterization of bonded joints under pure mode I loading. *Compos Sci Technol.* 68, pp. 2224-2230. DOI: 10.1016/j.compscitech.2008.04.003.
- [25] de Moura, M.F.S.F., Campilho, R.D.S.G., Gonçalves, J.P.M. (2009). Pure mode II fracture characterization of composite bonded joints. *Int J Solids Struct.* 46, pp. 1589-1595. DOI: 10.1016/j.ijsolstr.2008.12.001.
- [26] Anyfantis, K.N., Tsouvalis, N.G. (2012). A novel traction–separation law for the prediction of the mixed mode response of ductile adhesive joints. *Int J Solids Struct.* 49, pp. 213-226. DOI: 10.1016/j.ijsolstr.2011.10.001.
- [27] Abaqus®. Documentation of the software Abaqus®. Dassault Systèmes. Vélizy-Villacoublay 2013.
- [28] Shahverdi, M., Vassilopoulos, A., Keller, T. (2013). Modeling effects of asymmetry and fiber bridging on Mode I fracture behaviour of bonded pultruded composite joints. *Eng Fract Mech.* 99, pp. 335 - 348.
- [29] Ameli, A., Papini, M., Spelt, J.K. (2010). Fracture R-curve of a toughened epoxy adhesive as a function of irreversible degradation. *Materials Science and Engineering: A.* 527, pp. 5105-14. DOI: 10.1016/j.msea.2010.04.099.
- [30] Pardoën, T., Ferracin, T., Landis, C.M., Delannay, F. (2005). Constraint effects in adhesive joint fracture. *J Mech Phys Solids.* 53, pp. 1951-1983. DOI: 10.1016/j.jmps.2005.04.009.
- [31] Badulescu, C., Cognard, J.Y., Créac’hcadec, R., Vedrine, P. (2012). Analysis of the low temperature-dependent behaviour of a ductile adhesive under monotonic tensile/compression–shear loads. *Int J Adhes Adhes.* 36, pp. 56-64. DOI: 10.1016/j.ijadhadh.2012.03.009.
- [32] Zhao, B., Lu, Z.-H., Lu, Y.-N. (2014). Two-dimensional analytical solution of elastic stresses for balanced single-lap joints—Variational method. *Int J Adhes Adhes.* 49, pp. 115-126. DOI: 10.1016/j.ijadhadh.2013.12.026.
- [33] Reis, P.N.B., Antunes, F.J.V., Ferreira, J.A.M. (2005). Influence of superposition length on mechanical resistance of single-lap adhesive joints. *Compos Struct.* 67, pp. 125-133. DOI: 10.1016/j.compstruct.2004.01.018.
- [34] de Castro, J., Keller, T. (2008). Ductile double-lap joints from brittle GFRP laminates and ductile adhesives, Part I: Experimental investigation. *Compos: Part B.* 39, pp. 271-281. DOI: 10.1016/j.compositesb.2007.02.015.
- [35] Jiang, W., Qiao, P. (2015). An improved four-parameter model with consideration of Poisson’s effect on stress analysis of adhesive joints. *Engineering Structures.* 88, pp. 203-215. DOI: 10.1016/j.engstruct.2015.01.027.
- [36] Vable, M., Reddy Maddi, J. (2006). Boundary element analysis of adhesively bonded joints. *Int J Adhes Adhes.* 26, pp. 133-144. DOI: 10.1016/j.ijadhadh.2004.12.003.
- [37] Luo, Q., Tong, L. (2007). Fully-coupled nonlinear analysis of single lap adhesive joints. *Int J Solids Struct.* 44, pp. 2349-70. DOI: 10.1016/j.ijsolstr.2006.07.009.
- [38] Grant, L.D.R., Adams, R.D., da Silva, L.F.M. (2009). Experimental and numerical analysis of single-lap joints for the automotive industry. *Int J Adhes Adhes.* 29, pp. 405-413. DOI: 10.1016/j.ijadhadh.2008.09.001.
- [39] da Silva, L.F.M., Carbas, R.J.C., Critchlow, G.W., Figueiredo, M.A.V., Brown, K. (2009). Effect of material, geometry, surface treatment and environment on the shear strength of single lap joints. *Int J Adhes Adhes.* 29, pp. 621-632. DOI: 10.1016/j.ijadhadh.2009.02.012.
- [40] Davis, M., Bond, D. (1999). Principles and practices of adhesive bonded structural joints and repairs. *Int J Adhes Adhes.* 19, pp. 91-105. DOI: 10.1016/S0143-7496(98)00026-8.